STELLAR OCCULTATION LIGHTCURVE MODELING FOR ELLIPTICAL OCCULTING BODIES

by

Bryan Hilbert

B.A. Astronomy and Physics
Boston University, 1999

Submitted to the Department of Earth, Atmospheric, and Planetary Sciences
In partial fulfillment of the requirements for the degree of

Master of Science in Planetary Science
At the
Massachusetts Institute of Technology

September 2001

Signature of Author: .....
Department of Earth, Atmospheric and Planetary Sciences
August 10, 2001

Certified by:.....
James L. Elliot
Professor of Planetary Science and Physics
Thesis Supervisor

Accepted by:.....
Ronald G. Prinn
Head of Department of Earth, Atmospheric and Planetary Sciences

STELLAR OCCULTATION LIGHTCURVE MODELING FOR ELLIPTICAL OCCULTING BODIES

by

Bryan Hilbert

Submitted to the Department of Earth, Atmospheric, and Planetary Sciences
On August 10, 2001, in Partial Fulfillment of the
Requirements for the Degree of Master of Science in
Planetary Science

ABSTRACT

We present a new method of calculating model lightcurves for stellar occultations by the Jovian planets. We model the occulting planet as a three-dimensional body of non-zero ellipticity, and define two ellipses of intersection with the body which dictate the appearance of the lightcurve. These include the visible-limb plane ellipse, which is the observed figure of the body as seen in the sky, and the line-of-sight ellipse, which contains the line of sight to the occulted star, and is the plane in which the starlight is refracted. The observed stellar flux during the occultation is primarily dictated by the ellipticity and subsequent radius of curvature of the instantaneous ellipse in the line-of-sight plane. This new method is applied to several test cases, as well as to the Jovian occultation of HIP9369 on 10 October 1999. Lightcurves generated by this model are compared to identical situations using the method published in Hubbard *et al.* (1997), showing that the Hubbard model works well for low-latitude occultations, but fails at higher latitudes. In the case of the high-latitude Jovian occultation, the best-fit lightcurve, produced from this new method, yielded a half-light equatorial radius of 71,343±1.2 km with a scale height of 19.25±0.5km, and an isothermal temperature of 139K. The same data, fit using a lightcurve generated by the method described in Hubbard *et al.* (1997), resulted in a half-light equatorial radius of 71,819km with a scale height of 17.9km with errors comparable to the previous fit, resulting in an isothermal temperature of 129K. Lightcurves are numerically generated for an ellipsoidal planet and, for comparison, an approximation to the ellipsoidal case consisting of a sphere with radius equal to the radius of curvature of the ellipsoid at the half-light point. We find that in the case of an occultation where the line-of-sight ellipticity does not vary, that the radius of curvature approximation matches the ellipsoidal planet lightcurve to within 0.007%. For an oblique occultation however, the line-of-sight ellipticity varies, and the approximation, using only a single radius of curvature sphere, is only good to about 1%. As a result, we find that using a model such as that presented in Baum and Code (1953) to fit the lightcurve of an ellipsoidal planet can return values for half-light radius (after

accounting for the distance between the center of curvature and the center of the body) which may match the local distance to the center of the ellipsoid to a fraction of a percent, while returning values of scale height which may be in error by several percent. Test cases are also then put through numerical inversions, to obtain temperature versus pressure profiles. Test cases with spherical planets return temperature profiles that match those used to create the lightcurves, while test cases with ellipsoidal planets return temperature profiles which can differ from the input temperatures by tens of degrees, assuming a constant local gravity over the course of the occultation.

Thesis Supervisor: James Elliot
Title: Professor of Planetary Science and Physics

INTRODUCTION

One of the principal methods by which astronomers today learn about the atmospheres of solar system bodies is through the observation of stellar occultations. These events, in which a body passes in front of a star as seen from Earth or spacecraft, can yield a wealth of information about the occulting body's atmosphere simply from a continuous measurement of the flux of the background star as it is occulted. A plot of this stellar flux versus time over the course of the occultation is called a lightcurve. Evaluating the exact manner in which the flux changes with time during the immersion and emersion of the star can lead to estimates for the temperature, pressure, density, and refractivity of the occulting body's atmosphere provided knowledge of the geometry of the body and the distance of the body from Earth. This comes about through a complex method of analysis, which is the focus of this paper.

One of the primary methods of stellar occultation analysis is comparison of an observed lightcurve with that generated by a model. By matching the model lightcurve to the data, certain physical properties of the occulting body's atmosphere can be approximated by the model parameters used to create this best fitting model. However, this method relies on the accuracy of the model in creating the synthetic lightcurve to produce accurate estimates for the various calculated atmospheric parameters.

Some of the first atmospheric models (Baum and Code 1953) assumed a spherical occulting body with an isothermal atmosphere in calculating synthetic lightcurves. Since those first models were introduced, a number of improvements have been made in lightcurve generation models, including some which make corrections to allow for an elliptical occulting body (e.g. Hubbard *et al.* 1997; Cooray *et al.* 1998). The goal of this project is to develop a new lightcurve generation model aimed at properly taking into account the effects of an elliptical occulting body. A number of works in the past have attempted to take into account the ellipticity of the occulting body.

Hubbard *et al.* (1997), used zonal wind profiles to establish the limb shape of the occulting planet. A number of concentric bodies of this shape were then created. The passing light rays were then modeled in such a way as to identify the smallest of these concentric bodies that the light rays passed through. The equatorial radius of this smallest body was then entered into the flux equation derived by Baum and Code (1953) (Equation (1)), regardless of the latitude at which the occultation took place. In Cooray *et al.* (1998), lightcurves are calculated for Saturn by calculating the radius of curvature at the half-light point in the plane containing the center of the planet and the line of sight. There is no mention of what ellipticity is used in this calculation, or if it is different than the body ellipticity.

In the new model described here, we attempt to better account for the effects of an elliptical occulting body in order to calculate more accurate parameters to insert into the flux equations described below. The major changes in this new model are largely geometrical and include: 1) definition of a "visible-limb" plane such that it contains all limb points as seen by the observer. 2) definition of the "line-of-sight" plane for a given stellar position such that it contains the position of the center of curvature in the visible limb plane associated with the star's position, and the line of sight. (As opposed to Cooray *et al.* who use the center of the planet rather than the center of curvature in the sky plane) 3) refraction of the incident flux is controlled by the instantaneous radius of curvature of the planetary limb in the line of sight plane rather than the by the true radius.

Past Method and Equations

In order to produce a model lightcurve to compare with a measured lightcurve, there are in fact two separate aspects that must be considered. The first of these simulates the manner in which passing light rays are affected by the atmospheric shape (e.g. cylinder, sphere, ellipsoid) of the occulting body. The second is the density structure of the occulting body's atmosphere. Combining the geometrical shape and the density structure, the resulting expressions can be used to calculate a lightcurve for an occultation of a given planet. Current methods used for calculating model lightcurves are described in Chamberlain and Elliot (1997), Elliot and Olkin (1996), Elliot and Young (1992), and Hubbard *et al.* (1997). The code developed for this project is based on the method described in Chamberlain and Elliot (1997), which in turn is based on the model developed in Baum and Code (1953), with minor modifications. A brief summary of the final equations is presented below. For a more complete derivation, see Baum and Code (1953), and Chamberlain and Elliot (1997).

First, we consider the model describing the manner in which passing light is affected by the occulting body's atmosphere. As starlight from the occulted star passes the occulting body, three separate processes act to modify this light, affecting the flux that will be recorded by an observer. The first is a bending of the incoming starlight due to the refractivity of the gases in the atmosphere. The second is a focusing of the starlight resulting from the curvature of the planet's limb in the visible limb plane. Finally, as starlight is traveling through the planet's atmosphere, it may be attenuated through scattering and absorption. The first step in designing a model to describe the flux seen by an observer is to relate these three effects to the original starlight. Bending due to refractivity of the gases in the atmosphere is called refractive spreading and is diagramed in Figure 1. In refractive spreading, two light rays initially a distance dr apart will spread in the direction normal to the gradient of the refractivity in the occulting body's atmosphere, until they reach the observer. At this point, the spreading of the rays will cause them to be separated by some distance

$d\rho$. Differential bending will therefore expand the stellar flux in the observer's plane by a factor of $d\rho/dr$. In a similar fashion, focusing of the starlight by the limb of the planet will concentrate the flux by a factor equal to the ratio of the circumference of circle of radius r to the circumference of circle of radius ρ. For the case of a planet of large r, this ratio (~0.002 in the case of Jupiter) will be negligible compared to 1. Focusing effects are therefore neglected in the development of this large planet model.

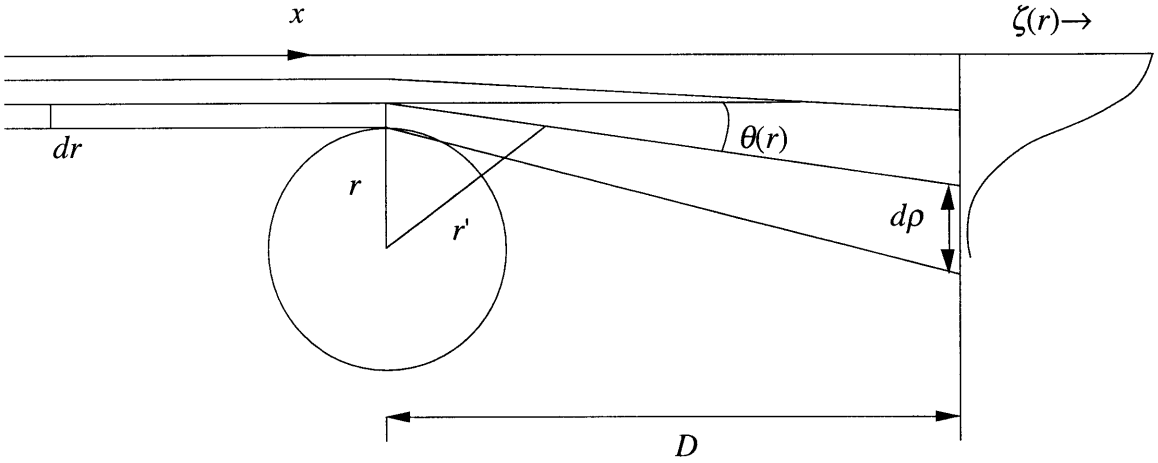

Figure 1: Refractive spreading of incident flux during an occultation. *D* is the distance from the occulting body to the observer, *r* is the radius of the occulting body, θ is the bending angle of the light rays, *dr* is the initial separation of 2 light rays, $d\rho$ is the final distance between the same light rays, and ζ is the observed flux, measured as a function of the depth in the occulting body's atmosphere.

Extinction can also be neglected, as discussed in Baum and Code (1953) due to the fact that the very low (~μbar) pressures in which the occultation occurs, the gases in the atmosphere cause significant refractive spreading of the incident starlight before enough molecules are encountered to cause notable extinction.

As derived in Baum and Code (1953) for an occultation occurring with constant relative velocity between the observer and the occulting body, the effects of refraction on the incident starlight produce an observed lightcurve which can be described by Equation (1), where ϕ_o is the value of the flux from the unocculted star, a is the inverse of scale height, v is the velocity of the observer with respect to the occulting body, t is the time, and ϕ is the instantaneous flux at a given time.

$$\left(\frac{\phi_o}{\phi} - 2\right) + \ln\left(\frac{\phi_o}{\phi} - 1\right) = avt \qquad (1)$$

Chamberlain and Elliot (1997) modify this equation slightly, replacing the dependence on observer velocity with one on the position of the star with respect to time. This new version of Equation (1), which is the basis for the lightcurve model developed in this work, is given by Equation (2).

$$-\left(\frac{1}{\phi} - 2\right) - \ln\left(\frac{1}{\phi} - 1\right) = \frac{y(t) - y_h}{H} \qquad (2)$$

In this new equation, *1/a* has been replaced by H, the scale height, and ϕ_o has been replaced by 1, on the condition that Equation (2) works only in the case where the observed lightcurve has been normalized by the value of the unocculted stellar flux. The parameter y_h is the distance of the half-light surface from the center of the planet's shadow, while *y(t)* is the distance of the occulted star from the center of the planet at time *t*. Values of *y(t)* much larger than y_h result in a flux very close to 1.0, while values of *y(t)* much smaller than y_h result in fluxes which approach zero. Setting *y(t)* equal to y_h, meaning that the position of the star is exactly on the half-light surface, we see that ϕ is 0.5, as expected.

This leads to the second model involved in calculating an occultation lightcurve. We need to create a model atmosphere of the occulting planet in order to perform the calculations described in Equation (2). For the model described above, a simple atmospheric model is all that is needed. With no effects of ellipticity included above, the atmospheric model that is used in conjunction with Equation (2) must be a spherical occulting body with designated constant scale height *H* and half-light radius y_h. These equations and inputs form the basis of the lightcurve model formulated in this work, with some changes in the generation of model inputs designed to take into account an occulting body of non-zero ellipticity.

Upon the successful creation of a model lightcurve matching an observed lightcurve, the next step in data analysis is often an inversion of the observed lightcurve. The purpose of inverting a lightcurve, as is discussed in detail in French *et al.* (1978), is to calculate temperature, scale height, and density profiles of the occulting body's atmosphere. The inversion procedure can be highly

sensitive to initial conditions. As a result, an observed lightcurve must be accurately modeled before inversion begins in order to provide the inversion procedure with a set of useful initial conditions. More specifically, the measured lightcurve is accurately fit by a model, down to a particular reference flux level. Often this reference point is the half-light point. The parameters of the best model fit at the half-light point are then taken as the initial conditions to be entered into the inversion procedure. For this reason, an accurate model is desirable in terms of minimizing inversion error.

Present inversion code, like that previously used for lightcurve modeling, also works on the assumption of a spherical occulting body. This investigation does not consider the changes necessary to directly modify the inversion procedure to account for an elliptical occulting body. Instead, the model lightcurves generated for the test cases described below were inverted using the present inversion code. Through a comparison of the output temperature profiles with those of the atmospheres used to create the model lightcurves, a sense of the errors in the inversion procedure for an elliptical occulting body can be found. The purpose behind this work was to find situations in which the present inversion code might work for an elliptical occulting body. At the very least, we wished to find situations with the elliptical body where the errors introduced in the inversion procedure for a spherical atmosphere showed patterned behavior, such as increasing errors with latitude of the occultation.

Observational Inspiration

The motivation behind this project arose from the occultation of the star HIP9369 by Jupiter on 10 October 1999. We observed both immersion and emersion of the star from the IRTF on Mauna Kea, as well as at WIRO (Wyoming InfraRed Observatory). At the IRTF, data were obtained in both near-IR (2.11 microns) and visible (0.89 microns) wavelengths, using NSFCAM in MovieBurst Mode, and MIT's Portable CCD (PCCD) system, respectively. Data at near-IR wavelengths (2.2 microns) were obtained at WIRO. Analysis began with the near-IR immersion data from the IRTF, as this data set had the highest signal to noise ratio of any of our observations.

These data consist of a series of images, taken at a rate of 4 Hz, for the duration of the immersion event. Photometry on the 1500 individual frames resulted in a measurement of the flux from HIP9369 over time, which is graphically represented as a lightcurve. The lightcurve from the immersion event recorded by NSFCAM is shown in Figure 2 where the dots represent the observed data points. Details of the method of photometry, creation of the lightcurve, and subsequent analysis of the data will be presented in a future paper, as the scope of this paper is a description of the generation of a new lightcurve modeling method.

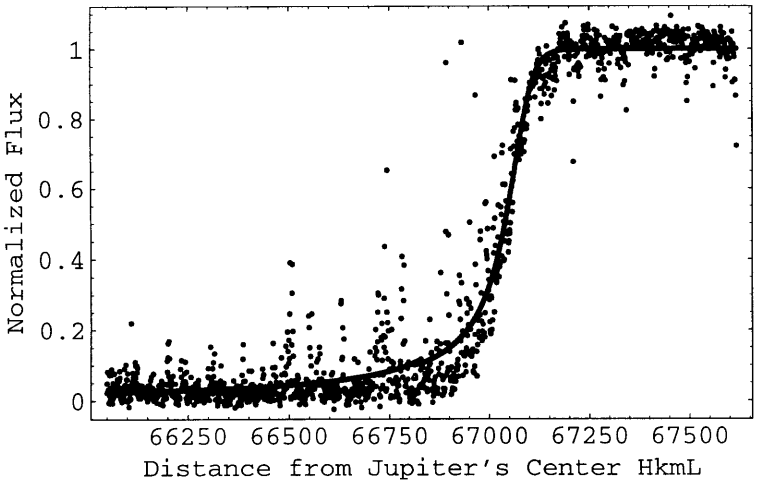

Figure 2: Lightcurve from the Jupiter occultation. The line passing through the data is the best-fit model lightcurve using the new method described in the following sections.

NEW MODEL DEVELOPMENT

Assumptions

The basis of our modified method for calculating stellar flux from the occulted star was the use of "radii of curvature" when generally speaking of the radii affecting the refraction, rather than true radii, which had been used in the past (see, for example Roques *et al.* 1994). This difference affects lightcurves only where the occulting body is elliptical rather than spherical. With Jupiter's non-zero ellipticity however, we believed that this change in parameter would have a noticeable effect on the model lightcurves. The reasoning behind using the radius of curvature comes from the assumption that the distance covered by a single immersion or emersion event is small compared to the radius of the planet. In using the radius of curvature, we assume that the properties of the

occulting body's atmosphere at the point of interest behave as they would in a sphere of equivalent radius. This makes intuitive sense, as the layers of the local atmosphere will follow the local curvature of the limb. Looking locally then, this situation appears identical to that in which we have a sphere of radius equal to the radius of curvature of the limb, as seen in Figure 3. In this respect, the radius of curvature appears to be a more appropriate distance to use in describing the properties of the atmosphere at some localized limb point. Moreover, since the incident solar flux is modified as it is traveling in the line of sight direction, it follows that we are interested in local atmospheric layers in the line of sight direction. Therefore, the equivalent sphere in which we are most interested is that which has a radius equal to the radius of curvature of the local limb in the line of sight direction.

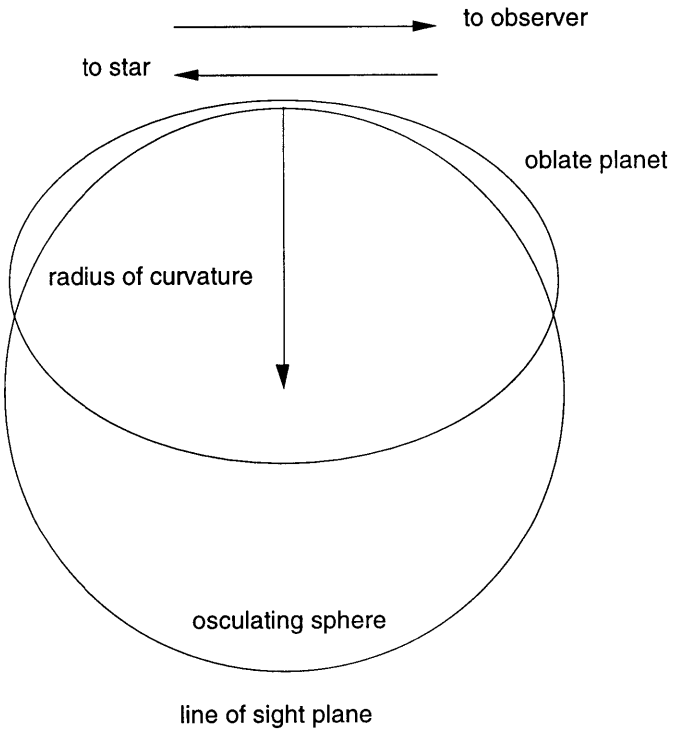

Figure 3: For a given occultation path of a star, an osculating circle was found in the line-of-sight plane, being tangent to the local limb of the elliptical planet. A lightcurve was then generated using this circle as an effective occulting planet.

3D Ellipsoid: Assumptions and Overview

We begin by examining the list of assumptions used in past lightcurve modeling, and choosing which of these assumptions we wish to use in our elliptical modeling. The following assumptions are used in our elliptical lightcurve generation model: 1) the shape of the occulting body's atmosphere is an oblate ellipsoid, 2) the observed occultation probes an atmospheric radial range small compared to the radius of the planet, 3) refraction of the starlight passing through the occulting planet takes place completely in a single plane defined as the visible limb plane (shown in Figure 1), 4) extinction over the occultation path is negligible, 5) the flux contribution from the far side of the occulting planet is negligible. With these assumptions in hand, we can develop our lightcurve generation model with an oblate ellipsoid. Equations are generated which fully describe the surface of this ellipsoid given values of equatorial radius a, and eccentricity e. For convenience, the program is written such that the position of the star relative to the center of the occulting body is input in (f,g,h) coordinates, as has been done in numerous past occultation studies (for example, Elliot *et al.* 1993; Cooray *et al.* 1998), where f is east, g is north, and h is normal to f and g and lies in the direction from the observer to the occulted star. Keeping in mind that the refraction of incident starlight within a planetary atmosphere occurs in the plane containing the line of sight, we see that an important characteristic to know is the local curvature of the occulting body's limb in the plane containing the incident flux. As a result, the first goal of the new model was to calculate the ellipticity of the occulting body in the line of sight plane for a given position of the occulted star. This was accomplished through a series of steps.

The first step is to place the body in any orientation with respect to the observer, and to do this using common parameters, which could be calculated for a given occultation. In the Astronomical Almanac, the polar positions of major planets are described by two numbers. The first of these numbers, symbolized by P, is the position angle of the north pole, measured north through east. The second number, commonly referred to as B, is the planeto-centric sub-Earth latitude. Using these two numbers, the exact orientation of the occulting body can be calculated at any time. Incorporating these two factors into the equation for an ellipsoid, we arrived at Equation

(3), with the relevant substitutions given in Equations (4) through (7). This equation is valid in an *(x, y, z)* coordinate system whose origin is at the center of the occulting body, where *z* points to the north, y points to the west, and *x* is the distance from the center of the body in the direction of the observer. Given equatorial radius, *a*, along with values for *e*, *P*, *B*, and an *x,y* point, Equation (3) returns the corresponding *z* points on the surface of the rotated ellipsoid.

$$z_{ellipsoid} = \frac{A_1 \pm 4(e-1)\sqrt{A_2 + A_3}}{A_4} \tag{3}$$

$$A_1 = 2e(e-2)(yCos^2(B)Sin(2P) - xCos(P)Sin(2B)) \tag{4}$$

$$A_2 = (a^2Cos^2(P) - y^2)(Cos^2(B) + (e-1)^2 Sin^2(B)) + (e-2)exySin(2B)Sin(P) - x^2Cos^2(P) \tag{5}$$

$$A_3 = \frac{Sin^2(P)}{2}\left(2a^2(e-1)^2 - x^2(2 + e(e-2)) - ex^2(e-2)Cos(2B)\right) \tag{6}$$

$$A_4 = (e-2)e\left(Cos(2B) + 2Cos^2(B)Cos(2P)\right) - 3e(e-2) - 4 \tag{7}$$

The next step in our method of calculating the ellipticity in the line of sight plane is to define the visible limb plane. This plane is very similar to the "sky plane" used in past occultation studies (for example Elliot *et al.* 1993). The sky plane has traditionally been defined as the plane perpendicular to the instantaneous line of sight, with the intention that the sky plane contains the limb points of the occulting body which are visible to the observer. However, one of the effects of an oblate occulting body is that in cases where the latter condition is true, the former may not always be true. In this respect, the visible-limb plane is defined through the locus of all limb points visible to the observer. For a given rotation, the visible-limb plane is not necessarily perpendicular to the line of sight due to projections resulting from the flattening of the body. For example, using a body similar to that of Jupiter (a = 71,500, e = 0.0649), and tipping the planet forward by 5 degrees, the northern- and southern-most positions of the ellipsoid in the visible limb plane deviate from the plane normal to the line of sight by 780 kilometers, yielding value of line-of-sight ellipticity, e_f ,equal to 0.0642. Increasing the forward rotation of the planet to 45 degrees results in the visible-limb plane containing points on the surface of the ellipsoid as far as 4,600 kilometers

from the plane normal to the line of sight. This results in an e_f of 0.0297 for the same body ellipticity e, of 0.0649. Equation (3), along with its partial derivatives with respect to x and y, allows the definition of the visible-limb plane. This is done by taking the partial derivative of Equation (3) with respect to x, and setting it equal to zero. Then, by also setting the y (east-west) values in the equation equal to zero, and solving the equation for x, we get the points on the ellipsoid at $y = 0$ where the slope of z with respect to x is zero. We then repeat this procedure with the y derivative of Equation (3). Setting $x = 0$, and solving for y, we get the points on the limb where $x = 0$ that have a slope of z with respect to y equal to zero. This gives us a total of four points on the limb of the occulting planet. Using any three of these points, an equation for the visible-limb plane can be generated. Given three points, with coordinates (x_1,y_1,z_1), (x_2,y_2,z_2) and (x_3,y_3,z_3), and the x and y components of any point of interest, the z component of this point of interest in the visible-limb plane, is described by Equation (8), where the index is cyclic.

$$z_{plane}(x,y) = \frac{\sum_{j=1}^{3}\left[z_j\left(x(y_{j+2}-y_{j+1})+y(x_{j+1}-x_{j+2})\right)+x_j\left(y_{j+2}z_{j+1}-y_{j+1}z_{j+2}\right)\right]}{\sum_{j=1}^{3}\left[x_i\left(y_{j+2}-y_{j+1}\right)\right]} \tag{8}$$

The ellipticity of the ellipse created by the intersection of the visible-limb plane with the occulting body is then found. Solving Equations (3) and (8) for x, setting them equal, and solving for y, we obtain an expression for the intersection between the ellipsoid and the visible-limb plane. This expression is presented in the Appendix, and will be subsequently referred to as Equation A. For a given value of z, Equation A gives the corresponding y value on the ellipse of intersection. Then, knowing y and z, the associated x component of the intersection point can be found through solving Equation (8) for x. Using this method, the ellipticity of the body in the line of sight plane, e_f, is calculated numerically by starting with a grid of equally spaced points in the north-south direction across a distance equal to the equatorial diameter of the occulting body. This assures that the occulting body is completely sampled around its limb, regardless of its orientation. Once the value of e_f is known for a particular planetary orientation, the center of curvature in the visible-limb

plane associated with a given stellar limb position is calculated through Equations (9) and (10), where the ellipse has been rotated such that the x-axis is along the semimajor axis of the ellipse.

$$x_{center} = x - x\frac{y^2 + x^2(1-e_f)^4}{y^2 + x^2(1-e_f)^2} \tag{9}$$

$$y_{center} = y - \frac{y\dfrac{y^2 + x^2(1-e_f)^4}{y^2 + x^2(1-e_f)^2}}{(1-e_f)^2} \tag{10}$$

Once these calculations are complete, the line of sight plane is identified as containing the original stellar position, its associated center of curvature in the visible-limb plane, and the line of sight. As before, we know three points that are in the line of sight plane. Therefore, Equation (8) can be used to get the z component of any point with components x and y in the line of sight plane. Again setting Equation (8) equal to the Equation (3), describing the surface of the ellipsoid, and solving the resulting expression for y, we obtain an expression describing the elliptical intersection of the line of sight plane and the physical body ellipsoid. This expression is also presented in the Appendix due to its large size, and will be referred to as Equation B. Given values for the semi-major axis of the ellipsoid, a, as well as values for e, P, B, the positions of the three points defining the line of sight plane, and the x component of a point of interest, Equation B will return the y value of that point on the line of sight ellipse. The corresponding z value can then be found using Equation (8). As in the case with the visible limb plane, the line of sight ellipticity, e_l, can be easily calculated numerically once Equation B was known. The reasoning behind calculating the x, y, and z components of points on the line of sight ellipse in a different order than those on the visible limb plane ellipse is to maximize numerical resolution. The visible limb plane ellipse exists close to the yz-plane, while the line of sight ellipse exists close to the xy-plane. Therefore, a regular grid of points in the x direction more completely samples the line of sight ellipse in the y and z planes than an initial grid of z points similarly spaced and translated into x and y components. A grid of equally spaced z points, which must initially cover a distance equal to the full equatorial diameter of the planet in order to account for all possible geometries, in the case of small planetary rotations, has

the majority of its points fall outside the line of sight plane. This means that most of the grid does not contribute to the description of the line of sight plane, and the resolution of the plane is severely limited. However, with the initial grid of points spanning the x-direction, almost all of the points fall into the line of sight plane, regardless of the geometry of the occulting body, and therefore maximize the resolution. The same logic applied to the visible limb plane ellipse dictates that the initial grid of points exist in the z direction rather than the x direction.

Calculating the ellipticity of the line of sight ellipse, e_l, allows the radius of curvature in the line of sight plane, referred to as r_l below, of the stellar position to be found. Similar to the situation in the visible-limb plane, this is done by rotating the line of sight ellipse into the x-y plane, such that Equations (9) and (10) can be used to find the center of curvature, and find the distance from the center of curvature to the original star position. In Figure 4, the line of sight ellipse can be imagined by cutting the ellipsoid along the indicated line, and looking at the cross section. The important feature to note is that this intercepted ellipse does not necessarily have the same ellipticity as that of the oblate occulting planet.

With the calculation of the line of sight radius of curvature completed, the refractive spreading affecting the incident starlight can be properly calculated. A large-planet lightcurve model based on the work of Baum and Code (1953) is then used to calculate the lightcurve resulting from these radii of curvature, assuming an isothermal atmosphere of scale height H. The Baum and Code model, however, assumes a spherical occulting body. We therefore need the best spherical approximation to our situation to substitute into the Baum and Code (1953) Equation (2). We use the calculated radius of curvature in the line of sight plane as the radius of an effective sphere in the Baum and Code equations. Rather than choosing a single radius of curvature to create a single effective sphere, we create a different osculating sphere following the instantaneous radius of curvature for each stellar position. In this way, we accurately account for ellipticity by adopting a changing radius of curvature over the course of the occultation. Alternatively, past methods for approximating occultations by oblate planets, such as that described in Cooray *et al.* (1998), use a single osculating sphere with a radius equal to the radius of curvature at one point during the

occultation. However, as the planetary latitude of the stellar position changes during an occultation, the radius of curvature also changes, meaning that the use of a single osculating sphere (usually matched to the radius of curvature at half-light) to approximate the elliptical limb will become less accurate. For example, again using a planet similar to Jupiter (a = 71,500 km, e = 0.0649), and a high latitude occultation with a star path nearly tangential to the local observed limb (identical to the occultation of HIP9369 discussed above), the radius of curvature in the line of sight plane varies from 76,660 km to 75,230 km, a 2% variation. The effects that this change in radius of curvature has on the resultant lightcurve will be explored in more depth in the following section of numerical tests.

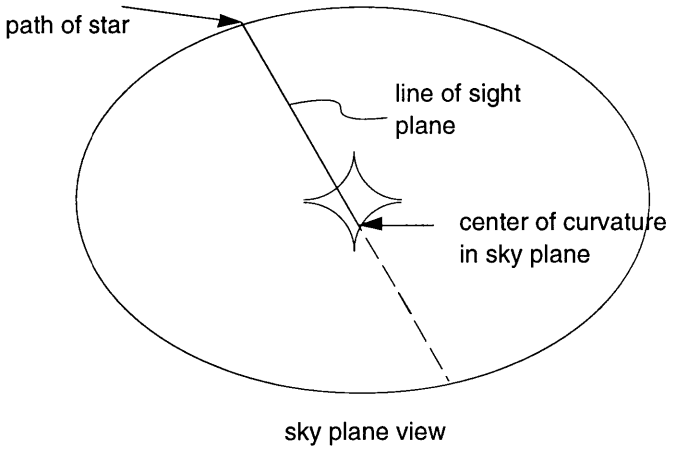

Figure 4: Definition of the line of sight plane. The diamond in the center is the loci of the center of curvature points associated with the limb points. The line passing through the diamond, combined with a line perpendicular to the paper, defines the line of sight plane.

MODEL TESTING

Numerical Integration Tests

In order to test whether developing such a complex model for an ellipsoidal occulting planet is worthwhile, we want to look at the real differences in lightcurves that result from using an ellipsoidal planet as opposed to a spherical planet. To this end, we generated a numerical model for creating lightcurves. This model is based on the equations presented in Chamberlain and Elliot (1997), where in this case, we choose to model the refractivity profile versus height. Using this

refractivity profile, we then propagate light rays through the model atmosphere numerically, creating an observed lightcurve. By modifying the refractivity profile in order to account for an ellipsoidal planet, we are able to create lightcurves for planets of arbitrary ellipticity. Given the numerical basis and the assumptions in this method, we are confident that the resulting lightcurves are accurate representations of the lightcurves that would be observed from planets of non-zero ellipticity.

The following test cases were generated in order to look at the effects of finite ellipticity on the appearance of the lightcurve. The first test case is spherical planet with a half-light radius of 66854.3 km and a scale height of 22.9235 km. The second is an ellipsoidal planet, similar in nature to Jupiter (a = 71,492 km, e = 0.06487), which has a polar radius of 66,854.3 km, and a scale height of 22.9235 km. The third is a spherical planet with radius equal to the radius of curvature at the pole of the ellipsoidal planet described above. In this case, the radius is 76,451.4 km, with the same scale height as in the cases above. Case numbers four and five are oblique occultations, meaning the path of the star is not perpendicular to the local limb of the planet, nor does it follow a line of constant latitude or longitude. Case four is an oblique occultation by a spherical planet, where the half-light radius of the planet is equal to the radius of curvature in the line-of-sight plane, associated with the ellipsoid in case 5. Case 5 is an oblique occultation by an ellipsoidal planet.

By numerically integrating these five test cases, we hoped to quantify the difference between lightcurves in the ellipsoidal case versus those of the spherical cases, both of which have been used in the past as approximations to lightcurves created from ellipsoidal planets. Polar occultations were simulated due to the fact that this is the situation in which the ellipticity of the planet should have the largest effect, as the ellipticity in the line of sight plane is equal to the body ellipticity. In this way, the error in assuming a spherical planet when the planet is truly ellipsoidal can be quantified.

Numerical integration of the ellipsoidal planet and the spherical planet in case 1, return two lightcurves that are in fact, very similar. The maximum difference in flux at any point along the lightcurve is only about 1.7%. This difference increases with the ellipticity of the ellipsoidal test planet. For example, using an ellipticity of 0.3, the difference rises to 8.9%.

Two lightcurve-generating models are then fit to these numerically integrated lightcurves. First, a simple Baum and Code model, following Equation (1) is fit to the lightcurves. This model is designed only for a spherical planet, so the fit to the lightcurve of the ellipsoidal occulting planet should only be an approximation to the true parameters of that lightcurve. The second model fit to the numerically integrated lightcurves is the ellipsoidal lightcurve model described in the preceding sections.

The fit results are shown below in Table 1. Fitting the Baum and Code model to the sphere in case 1 returns the exact half-light radius used in generating the lightcurve, and a scale height which is too large by 0.17%. Identical results are generated for case 1 when fitting the ellipsoidal model. From this, it appears that the numerical integration code works accurately, since both models match the integrated lightcurves well.

In case 2, the occulting planet is ellipsoidal. Fitting the Baum and Code model to the integrated lightcurve gives a best-fit half-light radius of 66,855.9km, which is larger than the radius used in the numerical integration by 1.6 km. However, fitting the ellipsoidal lightcurve model to the numerically integrated lightcurve, gives a half-light semi-major axis of 71,492 km, which corresponds to a polar radius of 66,854.3 km. This is exactly the radius used in the numerical integration.

In case 3, the radius of curvature at the pole is 9,597.1 km larger than the true polar radius. This type of sphere, making use of the radius of curvature of the true planet, is often used in modeling occultations by ellipsoidal planets, as it is a good approximation (ie Cooray *et al.* 1998). In this case, comparing the numerically integrated lightcurve of this sphere to that of the ellipsoidal planet, the lightcurves differ by no more than 0.007%. In this respect, this method of approximation, using the radius of curvature, seems effective. With such a close match to the lightcurve created by the oblate planet, fitting the Baum and Code and ellipsoidal models to this lightcurve returns identical results. The ellipsoidal lightcurve model returns a best-fit half-light radius of 66,854.3 km (after transforming the radius of curvature values back to real radius values by subtracting the appropriate distance listed above). This fitted radius is the distance used in

creating the numerically integrated lightcurve. However, as with the numerical lightcurve from the ellipsoidal planet, the Baum and Code model returns an adjusted half-light radius of 66,855.9 km, which is larger than the true half-light radius by 1.6 km.

	Numerically Integrated	Baum and Code model best-fit	Ellipsoidal model best fit
1) Polar occultation by a spherical planet with radius equal to the polar radius of case 2)			
a	66,854.3 km	66,854.3 ± 2.5×10^{-7} km	66,854.3 ± 4.5×10^{-7} km
H	22.9235 km	22.9274 ± 1.3×10^{-7} km	22.9274 ± 2.5×10^{-7} km
e	0.0	0.0	0.0*
2) Polar occultation by an ellipsoidal planet			
a	71,492 km (66854.3 polar radius)	66,855.9 ± 0.00001 km (polar radius)	71,492 ± 0.00003 km
H	22.9235 km	22.9274 ± 0.000008 km	22.9274 ± 0.00002 km
e	0.06487	0.0	0.06487*
3) Polar occultation by a spherical planet with radius equal to the radius of curvature of case 2			
a	76,451.4 km 66,854.3 km (adjusted)	76,452.9 ± 2.4×10^{-7} km 66,855.9 km (adjusted)	76,452.9 ± 4.5×10^{-7} km 66,855.9 km (adjusted)
H	22.9235 km	22.9269 ± 1.3×10^{-7} km	22.9269 ± 2.5×10^{-7} km
e	0.0	0.0	0.0*
4) Oblique occultation by a spherical planet			
a	72,909.7 km 67,694.9 km (adjusted)	72,909.7 ± 0.0001 km 67,694.9 km (adjusted)	72,909.7 ± 0.0001 km 67,694.9 km (adjusted)
H	23.5029 km	23.5062 ± 0.00005 km	23.5062 ± 0.00005 km
e	0.0	0.0	0.0*

5) Oblique occultation by an ellipsoidal planet			
a	71,492 km 67,694 km [1]	67,696 ± 0.03 km	71,492.7 ± 0.02 km
H	23.5029 km	24.3798 ± 0.02 km	23.1051 ± 0.01 km
e	0.06487	0.0	0.06487

Table 1: Comparison of fitted values of a (equatorial radius), H (scale height), and e (eccentricity), between those used to create a lightcurve through numerical integration, and those resulting from fits to those integrated lightcurves using the Baum and Code model, as well as the ellipsoidal light curve model. The elliptical case was created such that the polar radius was 66854.3 km. A * indicates that the quantity was not fitted, but was forced to be the indicated value. The center of curvature position in case 3) added a distance of 9597.09 km to the half-light radius. By subtracting this value from the fit results, a direct comparison with cases 1) and 2) is possible. The half-light radius of the numerically integrated lightcurve is then 66854.3 km, while both models fit to a half-light radius of 66855.9 km. [1] indicates the distance from the half-light point to the center of the ellipsoid.

The purpose behind cases 4 and 5 is to simulate occultations where the line of sight ellipticity is changing over the course of the occultation, in order to examine the differences created in the lightcurves for elliptical versus spherical planets. In case 4, as in the spherical case 1, the parameters in the numerical integration and those fitted by both models are identical. Also, similar to case 2, after the ellipsoidal planet case is numerically integrated, the ellipsoidal model fit returns parameters which are virtually identical to those used in the integration (see Table 1). The Baum and Code model however, returns parameters that do not match up as well. The model returns a half-light radius which is too large by 0.003%, and a scale height which is too large by 3.7%.

From these results, several conclusions can be drawn. First, from case 1, we see that in the case of a spherical occulting planet, the Baum and Code lightcurve model and the ellipsoidal model are both able to accurately fit the numerically integrated lightcurve, and return parameters equal to the parameters used as inputs in the creation of the lightcurve. Secondly, in the case of an elliptical occulting planet, , the Baum and Code model returns best fit parameters for the half-light radius and scale height which are larger than those used as inputs by 0.0024% and 0.017% respectively. The ellipsoidal model however, returns the exact parameters used in the numerical integration. Finally, a

sphere with radius equal to the radius of curvature of the ellipsoidal occulting planet at the pole is able to produce a very accurate approximation to the lightcurve computed directly from the ellipsoidal planet. However, as with the ellipsoidal planet, the Baum and Code model returned a half-light radius and scale height that are too large by 0.0024% and 0.017% respectively. The same is true of the ellipsoidal model in this case, when it is fit to this lightcurve with a forced value of 0.0 for ellipticity. However, with this lightcurve being a close approximation to that produced by the ellipsoidal planet, we expect the calculation of identical best-fit parameters from the ellipsoidal model when using the same ellipticity. Upon setting the ellipticity in the ellipsoidal model to 0.06487 and fitting the case 3 lightcurve, the model returns best fit parameters that are identical to those returned in case 2.

In comparing the numerically integrated lightcurves, as mentioned before, the difference between the lightcurves in cases 2 and 3 (ellipsoidal and radius of curvature sphere) is only 0.007%. These two cases are occultations where the line of sight ellipticity is constant. Making a similar comparison between cases 4 and 5, where the line of sight varies during the occultation, helps to illustrate the quality of the radius of curvature approximation to the ellipsoidal planet. In case 5, the line of sight ellipticity varies between 0.05561 and 0.05537, a 0.43% variation. Comparing the resulting lightcurve to that from case 4, we find a maximum difference between the lightcurves of 1.09%. It appears that when the line of sight ellipticity is not constant, using a sphere with radius equal to the radius of curvature is not as good an approximation as in the case where the line of sight ellipticity is constant. However, in terms of an observed occultation lightcurve, if the flux levels are not known to better than 1% accuracy, it appears that the radius of curvature approximation can be used without affecting the results.

Calculations: Test Cases

The oblate ellipsoid model is used to calculate lightcurves for a large number of test cases. First, the method is used on a spherical planet in order to confirm that the end results are the same as those produced with a simple Baum and Code (1953) model for generating lightcurves. Indeed, the new method produces a lightcurve for a spherical planet that exactly matches that calculated with the older method. Not surprisingly, these lightcurves, when put through the inversion code (which assumes a spherical occulting planet), create temperature versus pressure profiles which match those of the model atmosphere input into the lightcurve generator.

The next test cases involve a body of the same ellipticity as Jupiter, with no rotations, meaning that the polar axis is exactly north-south, and perpendicular to the line of sight. Immersions are simulated at seven different latitudes, including along the equator and down the polar axis. In all cases, the occultation path used is normal to the local limb, in order to minimize the differences in line-of-sight ellipticity over the course of the occultation, and allow e_l to be presented as a single number in the Table 2. If the test cases use non-radial motion, as was present in the observed Jupiter occultation, e_l would vary over the course of the occultation. In the case of Jupiter occulting HIP9369, which was a high-latitude, near-tangential event, e_l was calculated to vary between 0.0644 and 0.0617, a roughly 4.5% variation. As discussed previously, this variation in the line of sight ellipticity over the course of the occultation means that the use of a single radius of curvature sphere to approximate the ellipsoidal planet will not be as accurate as if the line-of-sight ellipticity is not varying. In the numerical integration test case using an oblique occultation of an ellipsoidal planet, if a Baum and Code model is used to model the lightcurve with a single, radius of curvature sphere, the best-fit half-light radius may be wrong by only hundredths of a percent, but the best-fit scale height may be wrong by several percent.. For each event, lightcurves generated using the new, ellipsoidal lightcurve generation method are shown in Figure 5.

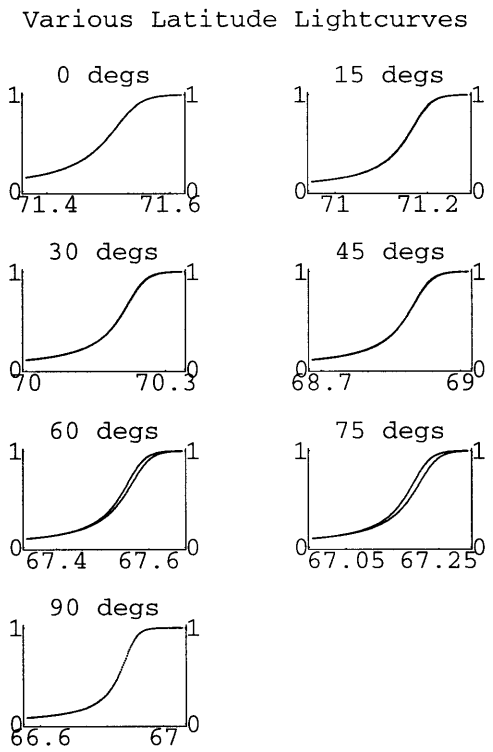

Figure 5: Lightcurves at seven different latitudes produced using both the new method of lightcurve generation described in this paper and the Hubbard *et al.* (1997) model. Each lightcurve is plotted as normalized flux versus distance from the center of the test body, in units of thousands of kilometers. In the plots where the two lightcurves are distinguishable, the lightcurve on the right is the one created with the new model described here. Note the increasing difference between the two methods with increasing latitude.

Comparison with Other Models

The next step is to compare these new lightcurves with some generated using an older method for the same geometry. For this purpose, the previous method of lightcurve generation consists of the model used by Hubbard *et al.* (1997), as this model is the most recent and sophisticated in dealing with ellipsoidal occulting bodies. For a complete description, see Hubbard *et al.* (1997). This model uses gravitational harmonics combined with wind profiles in order to calculate the potential at a given position relative to the center of the occulting body. In this way, the limb of the occulting body can be represented as an equal-potential surface. By taking the position of the occulted star relative to the limb of the occulting body at a given time, and propagating a ray of light from the star to the occulting planet, the surface of lowest potential that the light ray crosses

is identified. After accounting for gravitational bending and focusing, the equatorial radius of this lowest potential surface is then input into the Baum and Code lightcurve model shown in Equation (1). More specifically, the change in this equatorial radius with time in the reference frame where the occulting planet is stationary and the star moves relative to the planetary limb is used in Equation (1) as the velocity. As stated in Hubbard *et al.* (1997), this method is accurate only for low latitude occultations due to the fact that the equatorial radii are entered into the Baum and Code equation. It is therefore expected that the high-latitude lightcurves generated with this model differ significantly from our own.

For the seven test cases described above, we produce lightcurves using our method, as well as Hubbard's method. As expected, the low-latitude test cases produce identical or near identical lightcurves. At the higher latitudes, our lightcurves begin to deviate noticeably from those produced with the equal potential surfaces. This can be seen in Figure 5.

The next step is to manipulate the parameters in the equal potential model such that the lightcurves created match those produced by our model at all latitudes. In this way, the error in the physical parameter estimates derived from the equal potential model can be roughly quantified. The parameters input into the equal potential model include the scale height, the velocity of the occultation, (calculated from the change in equatorial radius with time as described above), and time relative to the half-light time. Two separate fits are made. In the first, the scale height is held constant, and time and velocity are allowed to vary. In the second, the velocity is fixed, while the scale height and time vary. The first gives results that make intuitive sense, as the velocities which allow the equal potential model to match our model are simply the change in star position with time (stellar velocity as described above), as opposed to the velocity of the equatorial radii. Since, in reality, it is the change in the star position relative to the planetary limb with time that controls the amount of observed flux, the fit of velocity to the stellar velocity is expected. At higher latitudes, where the two initial lightcurves differ the most, the difference between the equatorial radius velocity and the stellar velocity is the greatest. Basically, it is this difference in velocity which, when input

into the Baum and Code (1953) equations, causes the difference in the two methods of modeling lightcurves. In each case, there is also an offset of the half-light times, as seen in Table 2.

In the second fit, which more closely resembles the procedure that would be followed in the analysis of an observed lightcurve, the scale height is allowed to vary rather than the velocity. The lightcurves created with our elliptical occultation lightcurve model are all created with a scale height of 18.5 km, as preliminary analysis of the Jupiter occultation from above indicates a scale height of roughly this value. In fitting the lightcurves from the equal potential model, the scale heights for the high-latitude test cases are forced to change by up to 7% in order to create matching lightcurves. Taking this analysis one step further, the isothermal temperature of the atmosphere is given by $T = H \mu g / R$, where H is the scale height, μ is the molecular weight of the atmosphere, g is the local gravity, and R is the gas constant. From this, we see that the 7% error in the scale height translates to a 7% error in the estimated temperature of the atmosphere. Correspondingly, we see that at the higher latitudes, a significant error in the atmospheric scale height and temperature is present when using the equal potential lightcurve generator, as is stated in Hubbard *et al.* (1997). Details of the various fits are shown in Table 2 and described below.

The immersion along the equator is a special case, due to the fact that the line of sight plane is coincident with the equatorial plane, in the case where there was no rotation of the pole out of the visible-limb plane. As a result, the line of sight cut through the ellipsoid is in fact a circle as one looks down upon it from above the north pole. In this case, the situation becomes equivalent to that of a spherical planet. With the new, ellipsoidal lightcurve generation method, the lightcurve for the equatorial occultation is generated using an ellipticity of zero, as this was e_1 in this case. In addition, for the equatorial occultation case, the position of the star at any given time is at the equatorial radius of some equal potential surface. Therefore, in this case, the change in stellar position with time is exactly the same as the change in equatorial radius with time, and both lightcurve generation methods produce identical lightcurves. The same is true of the occultation along the polar axis. This is due to the fact that in order for our lightcurve model to simulate an occultation directly down

the polar axis, we have to turn the planet on its side, meaning that the polar occultation effectively becomes an equatorial occultation.

e = 0.06487,Half-Light Equatorial Radius = 71,492 km				Fit #1 (velocity and time vary)		Fit #2 (H and time vary)		
Immersion Latitude	Velocity of (f,g) Positions (km/sec)	Creation H (km)	Equatorial Radius Velocity (km/sec)	Time Shift (sec)	Fitted Equatorial Velocity (km/sec)	Fitted H (km)	Time Shift (sec)	Half-Light Equatorial Radius Difference From 71,492 km
0°	2.0	18.5	2.0	0	2.0	18.5	0	0 km
15°	2.0	18.5	2.01097	0.66	2.0	18.6	0.66	1.4 km
30°	2.0	18.5	2.04064	0.4	2.0	18.9	0.4	0.8 km
45°	2.0	18.5	2.08048	0.19	2.0	19.25	0.19	0.4 km
60°	2.0	18.5	2.11956	4.07	2.0	19.6	4.07	9 km
75°	2.0	18.5	2.12973	6.0	2.0	19.75	6.0	15 km
90°	2.0	18.5	2.0	0	2.0	18.5	0	0 km

Table 2: Fit results. Creation H and velocity of stellar position indicate the scale height and velocity used with the elliptical method to create the initial lightcurve. Velocity in this case is simply the change in the stellar position with time. For each test case, the equatorial radius velocity is also given. This is the change in the equatorial radii of the equal energy surfaces with time. In Fit #1, H was kept constant at 18.5 km, while the equatorial radius velocity and time were allowed to vary. The time shift column shows the difference in seconds between the half-light time in our model, and that in Hubbard's model. In Fit #2, the equatorial radius velocity was kept constant at the values in the second column, while H and time were allowed to vary. The last column shows the difference in km, between the equatorial radius used in the creation of the lightcurves (71,492 km), and that calculated using the model of Hubbard *et al.* (1997). These values were calculated using the time shifts and velocities. Keep in mind that all columns except the scale heights are relative to one another. If the position velocity in the second column were doubled, then the equatorial radius velocities, time shifts, and half-light equatorial radius differences would also double.

Elliptical Model Effects: Line of Sight Ellipticity Variations

Given that the line of sight ellipticity is important in lightcurve generation models, we wish to look at how this value changes for a given body. With the inspiration behind this project being the Jupiter occultation described above, we use an ellipsoid of e equal to 0.06487, comparable to

that of Jupiter. The first variation we wish to look at is how e_l varies with the latitude of the occultation. Again, test cases are generated in which the path of the star is in the radial direction, minimizing the variation in e_l over the course of the occultation. Again, all simulated occultations in this case are performed with no visible limb plane rotations of the planet. The line of sight ellipticity is seen to increase from zero, in the previously discussed equatorial occultation, to e, in the case of a polar occultation. In the polar case, the line of sight plane is that which contains the polar axis and the line from the star to the observer, which indeed intercepts the ellipsoid in an ellipse with the same ellipticity as the body ellipticity, e. From Table 2, the behavior of e_l is seen to be a non-linear function with latitude. At higher latitudes, e_l changes very little with increasing latitude, while at mid-latitudes, the change seems to be maximized.

Immersion Latitude	Line of Sight Ellipticity
0°	0.00000
15°	0.00610
30°	0.02112
45°	0.03835
60°	0.05272
75°	0.06181
90°	0.06487

Table 3: Line of sight ellipticity versus the latitude of the occultation for no rotation of a planet with body ellipticity e = 0.06487. Line of sight ellipticity is a non-linear function of latitude.

Extending this investigation to include the effects of forward rotation, the same calculations are repeated at multiple latitudes, with the occulting body tipped forward by various amounts. Rotation of the body in the visible limb plane is ignored, as this does not change the definition of the visible-limb plane or line-of-sight plane, yielding identical values of e_l as in the case of no rotation. Tipping the body forward however, can cause changes in the visible limb plane ellipticity, e_f, which will then cause the line of sight plane to be defined differently, as the center of curvature in the visible limb plane will vary. For each of the occultation latitudes, e_l is calculated for eight different forward rotations of the planet, up to 45°. The results of these calculations are shown in Figure 6. It is interesting to note that as the amount of rotation increases, e_l increases for all

latitudes and in fact, all appear to be converging on the value of the body ellipticity, *e*. This makes sense, as an equatorial occultation for a rotation of 90°, will have a line of sight plane which contains the star on the equator, and travels down the line of sight, which now contains the polar axis. This plane intersects the planet in an ellipse with ellipticity equal to the original body ellipticity, *e*. Since an equatorial occultation will always produce the line of sight ellipse with minimum ellipticity, as the equatorial situation moves towards *e* with increasing rotation, so must the occultations at other latitudes, as seen in Figure 6. This underpins the importance of both using e_l, and knowing the exact orientation of the occulting body when creating the lightcurve, as ellipticity can vary from zero up to the ellipticity of the body.

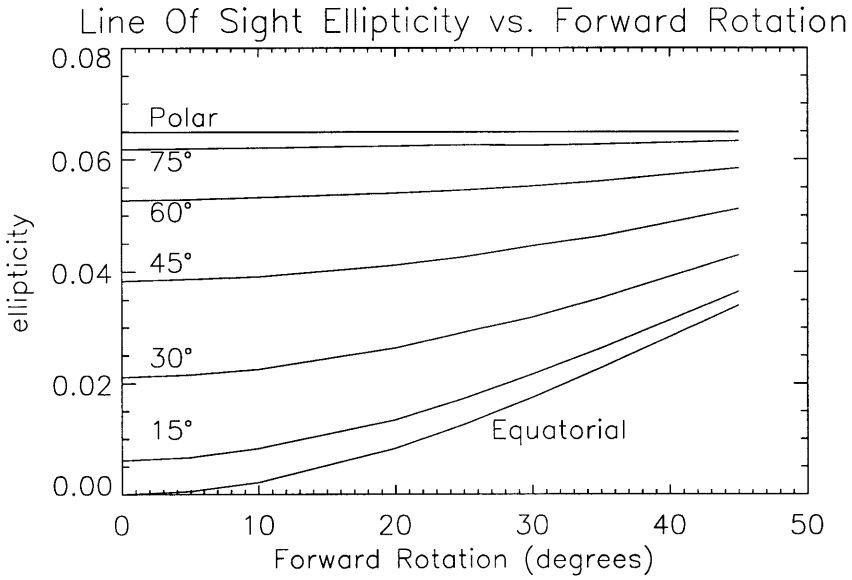

Figure 6: Line of Sight Ellipticity versus Forward Rotation angle. Lines represent occultations at a given latitude.

Jupiter Results

Following the test cases, the new lightcurve generation code is applied to the previously described Jupiter occultation. A least-squares fit is used to find the parameters for the best matching lightcurve to the immersion event observed at the IRTF. The resulting fit is shown in

Figure 2. Radii of curvature in the line of sight direction vary from 76,430 to 75,070 km, and line of sight ellipticity values range from 0.0644 to 0.0617. This lightcurve model, which is generated using a sub-Earth latitude of 3.82 degrees, a position angle of 338 degrees, and a body ellipticity of 0.06487 (USNO 1998), result in a half-light equatorial radius of 71,343 ± 1.2 km, and a scale height of 19.25 ± 0.5 km. From Equation (11), this corresponds to an isothermal temperature of 139 K (using the local gravity at the half-light altitude. Using the gravity at the deepest level probed by the occultation, the isothermal temperature is calculated as 143 K).

For comparison, the Jupiter data is fit using the Hubbard *et al.* model. Due to the fact that this particular occultation took place in the polar latitudes, we do not expect the Hubbard model to fit the data well. Upon fitting, the Hubbard model returns a half-light equatorial radius of 71,819 km, and a scale height of 17.9 km, both of which are outside the error bars of the values produced in the elliptical model fit. Similar to what is seen in Table 1, the value of 17.9 km is a 7% error in scale height, which leads to an isothermal temperature value of 129 K calculated through Equation (11). As expected, the Hubbard *et al.* model fits the high latitude occultation poorly.

INVERSION RESULTS

Upon inverting the test cases with no forward rotation, we compare the calculated temperature profiles with those used initially to create the model atmosphere. For all test cases, the lightcurves were generated with a 117K isothermal model atmosphere. This temperature value was calculated using the relation in Equation (11).

$$T = \frac{H\mu g}{R} \tag{11}$$

In this equation, H is the scale height, μ is the molecular weight, g is the local gravity, and R is the molar gas constant. Figure 8 shows the results of the inversion of the lightcurve generated for an equatorial occultation with no rotations of the occulting body. The left panel of Figure 7

shows the results of inverting the lightcurve using a radius scale calculated simply from geometric radii.

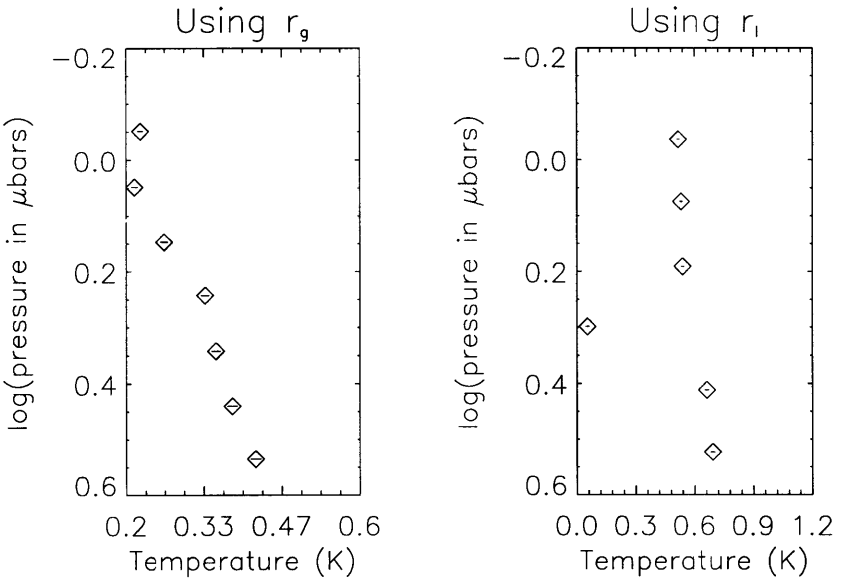

Figure 7: Inversion profiles for an equatorial occultation. The left panel is an inversion using radii of curvature derived from e_l, while the right panel used radii of curvature derived from e. The model atmosphere used to create the inverted lightcurve was isothermal at 117 K. Temperature scale on the left is Kelvins above 117K, while temperature scale on the right is Kelvins above 133K.

In the case of an equatorial occultation, $e_l = 0$, meaning geometric radii and radii of curvature will be identical. This is supported by the left panel of Figure 7, with the effectively isothermal inversion of the lightcurve at the desired temperature of 117 K. The right panel of Figure 7 shows the inversion results for the same lightcurve, but using radii of curvature calculated by setting $e_l = e$, the body ellipticity. Again, we see an effectively isothermal inversion, but at a value of temperature which is too high by 15%. From this, it appears that using the radii of curvature determined from e will cause errors in the inversion process similar to the way they caused errors in the lightcurve generation process.

From the above example of lightcurve generation and inversion for the special case of an equatorial occultation ($e_l = 0$), we see that the new method of generating lightcurves reduces to the original Baum and Code (1953) method of a spherical occulting body. We also see that the inversion procedure correctly inverts the lightcurve. Unfortunately, since the inversion code

assumes a spherical occulting body, the equatorial occultation was the only case in which the lightcurve inverted to isothermal at the correct temperature. At higher latitudes, e_l becomes non-zero, meaning that the inversion code attempts to invert a body of finite ellipticity as a sphere of radius equal to the given half-light radius. This leads to inversions of the newly created lightcurves that deviate from isothermal and the correct temperature. This effect is shown in Figure 8.

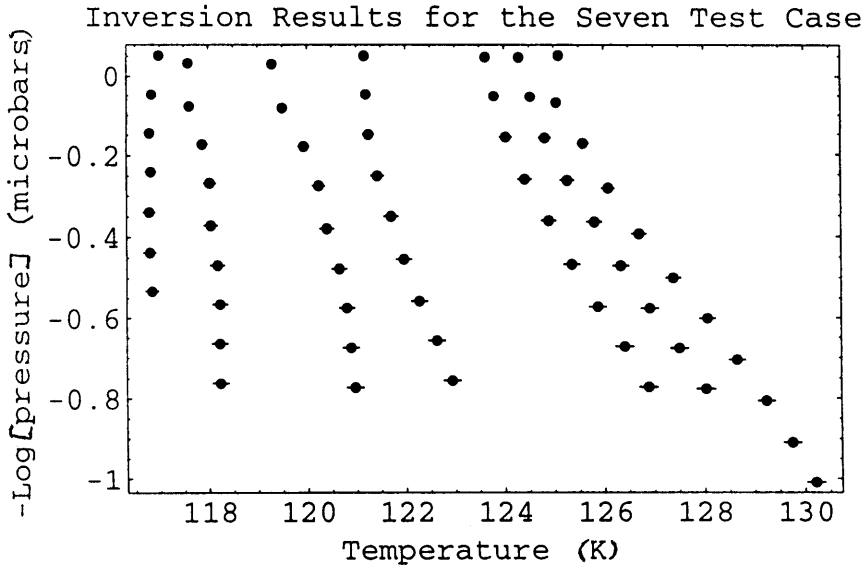

Figure 8: Inversion results for test cases of occultations at different latitudes of the same occulting body. From left to right, the temperature profiles are for occultations at: 0°, 15°, 30°, 45°, 60°, 75°, and 90°. The atmosphere used to create the lightcurves had a constant *H* = 18.5 km, which corresponds to 117K at the equator. Here we see that the overall temperature, as well as the temperature gradient, increases with increasing latitude, due to *g* increasing at higher latitudes on the half-light surface.

Figure 8 shows the corresponding temperature profiles obtained through inversion of the lightcurves shown in Figure 5. Upon inversion, the calculated temperature profiles differ from isothermal by varying amounts. In Figure 8 the temperature profiles are seen to differ from isothermal as well as the correct temperature of 117K by amounts which seem to increase with latitude. Knowing from Table 2 that e_l increases with increasing latitude, the fact that the error of the inverted temperature profile increases with increasing latitude is expected. With the inversion code assuming a spherical occulting body, higher latitudes correspond to ellipses that are farther from circular, causing larger errors in the inversion.

Returning to Equation (11), we can see the reason behind the increasing errors. Since we designate H as a constant, the only variable besides temperature in this equation is the local gravity.

The value of g in Equation (11), is calculated through the familiar relation $g = GM/r^2$, where G is the gravitational constant, M is the mass of the occulting body, and r is the distance from the center of the occulting body at which the local gravity is being calculated. Therefore, at the same atmospheric layer along different latitudes, the distance to the center of the body will vary, which will cause local gravity, and hence, temperature to vary. For this reason, the inversions of occultations at non-equatorial latitudes return temperatures that differ from the input isothermal temperature. From Equation (11), as the distance from the center of the body to the limb decreases, with all other parameters held constant, the temperature increases. This is confirmed in Figure 8, where the equatorial occultation inverts to the lowest temperature and the polar to the highest. In order to bring the isothermal temperature of non-equatorial occultations down, the value of H must decrease with increasing latitude in order to compensate for decreasing r. This makes physical sense, as the polar atmosphere is affected less by centrifugal force from the rotation of the body than the equatorial atmosphere, and therefore has a higher value of g. An increase in g will decrease the scale height at higher latitudes in order to keep the atmosphere isothermal. The exact changes that must be placed in the inversion procedure to account for this non-spherical behavior will be left to later study.

CONCLUSIONS

After extensive numerical modeling, we find that our new method of generating stellar occultation lightcurves through the use of an oblate ellipsoid as the occulting body, produces accurate lightcurves. The key to the generation of such lightcurves is the definition of the elliptical intersections of the visible-limb plane and the line-of-sight plane with the occulting body, along with their respective ellipticities. The appropriate ellipticity to use in the calculation of the lightcurve is the ellipticity of the ellipse contained in the line-of-sight plane, e_l, due to the fact that this is the ellipticity that dictates the radii of curvature in the plane in which the starlight is refracted. In terms

of modeling, this line-of-sight ellipticity is the value that controls the radii of curvature that can be used to create spherical approximations to the ellipsoidal occulting body.

Through our numerical integration tests, we show that in the cases where the line-of-sight ellipticity is not changing, an ellipsoidal occulting planet can be approximated by a spherical planet with a radius equal to the radius of curvature at the occulted star's position on the ellipsoidal planet. Generating the lightcurve from this equivalent sphere gives fluxes which are different from those produced by the original ellipsoidal planet by no more than 0.007%. In cases where the line-of-sight ellipticity does vary over the course of the occultation, the method of approximating the ellipsoidal planet by a spherical planet, using the radius of curvature, produces a lightcurve which can vary from that created by the ellipsoidal planet by as much as 1.1%. However, this is still a good approximation, unless the flux in an observed lightcurve is known to better than 1%. In the development of our model however, we wanted our errors to be as small as possible, and so, put to use the fact that the approximation is very good when the line-of-sight ellipticity doesn't change.

In order to maximize the accuracy of the radius of curvature approximation, the line of sight plane is redefined for each measured star position, as e_f will change for each line of sight cut through the ellipsoid. For an occultation such as that described above for Jupiter, where the angle between the path of the star and the local limb was very small, the line of sight ellipse will rotate and change ellipticity over the course of the occultation.

We also show that the exact orientation of the occulting body with respect to the observer must be known, as e_f can change significantly with rotation depending on the latitude of the occultation, as seen in Figure 8. Despite the fact that the rotation in the visible limb plane does not affect e_f, accurate knowledge of the visible limb plane rotation is also necessary in order to determine the latitude of the occultation. The center of curvature of the ellipsoid at the position of the star in the visible limb plane will vary dramatically depending on the entrance latitude of the visible limb plane ellipse. For a body with ellipticity and semi-major axis comparable to those of Jupiter, the center of curvature position for the star can be offset from the center of the body by as much as 9600 km. Accurate knowledge of the center of curvature point and the position of the star

along the planet's limb is vital because they determine the line of sight ellipse. With these changes to the method of lightcurve modeling, resulting temperatures and scale heights derived from lightcurve models more accurately reflect the characteristics of the occulting body's atmosphere.

Comparisons of this new model to that described in Hubbard *et al* (1997) are made using a variety of test cases. As seen in Figure 5, at low latitudes, our model produces lightcurves that are identical to those produced by Hubbard's method. However, as the latitude of the occultation increases, Hubbard's model becomes less accurate, as stated in Hubbard *et al* (1997). In Table 2, a head-to-head comparison of the model fits is shown. While all the lightcurves are originally created with scale heights of 18.5 km, there is a clear trend of increasing scale heights with latitude returned by Hubbard's model. At 75° latitude, Hubbard's model returns a scale height of 19.75km, a 6.75% error, along with a 6.0 second time shift, corresponding to a 12 km difference in half-light radius. These errors are expected however, since Hubbard's method is focused on velocities in the equatorial plane, rather than velocities at high latitudes.

Comparisons between lightcurves generated by numerical integration and the ellipsoidal model allow for the investigation of more fundamental questions. During this series of tests, we compared the results of our model to those produced by a Baum and Code model, which has been one of the basic models for calculating lightcurves for spherical planets for many years. To show that the generation of our ellipsoidal lightcurve model is valuable, we conducted numerous numerical integration tests. By numerically integrating the paths of light rays as they are passing through the occulting planet, we create accurate lightcurves that we can compare to one another, as well as fit with different models. Comparing a lightcurve from an oblique occultation by an ellipsoidal planet, with an oblique occultation by a spherical planet with the radius set equal to the radius of curvature in the ellipsoidal case, we find that the flux varies by 1.1%. This variation does cause a slight difference in the best-fit model parameters when models are fit to these lightcurves. The oblique ellipsoidal occultation has a varying value of line-of-sight ellipticity and therefore, radius of curvature, over the course of the occultation. Fitting the Baum and Code model to this oblique ellipsoidal occultation is equivalent to approximating the many values of radius of curvature

with a single sphere of one radius of curvature. In our numerical integration tests, this fit returned a half-light radius that was too large by only 0.003%, but a scale height that was too large by 3.7%. Meanwhile, fitting the ellipsoidal lightcurve model to this test case returned a half-light radius which was too large by 0.0009%, and a scale height which was too small by only 1.7%. Repeating this procedure for ellipsoidal and spherical occultations in which the line-of-sight ellipticity did not vary returned two numerically integrated lightcurves which differed only by 0.007%, and best-fit model parameters which all had errors less than 1%.

From this, we conclude that using a single radius of curvature to create a spherical planet in order to approximate the ellipsoid is a reasonable method of approximation, as long as the flux levels in the ellipsoidal light curve are known to no better than 1%. However, in the case of an ellipsoidal planet where the ellipticity and orientation are known, fitting the lightcurve using the ellipsoidal lightcurve model returns parameters with the smallest errors.

Finally, we look briefly at the effects of ellipticity on the inversion process. Current inversion code assumes a spherical occulting body and so, once ellipticity is accounted for in the generation of the lightcurve, we wish to see if it can be easily accounted for in the inversion of that lightcurve. We find that for low latitude occultations, where the line-of-sight ellipticity is close to zero, inversions of lightcurves produced from isothermal atmospheres return temperature versus pressure profiles that are isothermal at the correct temperature. However, as the latitude of the occultations increases, the returned temperature profiles become less and less isothermal, and trend towards increasing temperatures with depth. For example, as seen in Figure 8, the inversion of an occultation by a 117K atmosphere, at a latitude of 75° returns a temperature profile beginning at 126K and increasing with depth to 130K. This error in the temperature profile most likely results from the changing value of the local gravity over the course of the occultation, and may need to be addressed before further inversions of observed high latitude occultations.

APPENDIX

Equation A, as described in the text. In this, as well as in Equation B below, *a* is the equatorial radius, *e* is the body ellipticity, *b* is the sub-Earth latitude of the occulting planet, *P* is the position angle of the north pole, *xpt* is the x-coordinate whose corresponding *y* value you are searching for, and *x1, x23, x3, y1, y2, y3, z1, z2*, and *z3* are the xyz coordinates of three points defining the plane of intersection.

$$
\begin{aligned}
&\text{yintc} = \text{Compile}\Big[\{a, e, b, P, \{\text{xpt}, \_\text{Real}, 1\}, x1, x2, x3, y1, y2, y3, z1, z2, z3\},\\
&\Big(-2\,\text{xpt}\,((2-e)^2 e^2 \cos(P)\cos^2(b)\sin(2P)\sin(2b) - 2(e-2)(e-1)^2 e\sin(P)\sin(2b))(x2y1 - x3y1 - x1y2 + x3y2 + x1y3 - x2y3)^2 +\\
&\quad 4(2-e)e\,((\cos^2(b) + (e-1)^2\sin^2(b))\cos^2(P) + (e-1)^2\sin^2(P))\\
&\quad\quad ((x3y2z1 - x2y3z1 - x3y1z2 + x1y3z2 + x2y1z3 - x1y2z3 + \text{xpt}(-y2z1 + y3z1 + y1z2 - y3z2 - y1z3 + y2z3))\sin(2P)\cos^2(b) +\\
&\quad\quad\quad \text{xpt}(x2z1 - x3z1 - x1z2 + x3z2 + x1z3 - x2z3)\cos(P)\sin(2b))(x2y1 - x3y1 - x1y2 + x3y2 + x1y3 - x2y3) -\\
&\quad 8(x2z1 - x3z1 - x1z2 + x3z2 + x1z3 - x2z3)\\
&\quad\quad (x3y2z1 - x2y3z1 - x3y1z2 + x1y3z2 + x2y1z3 - x1y2z3 + \text{xpt}(-y2z1 + y3z1 + y1z2 - y3z2 - y1z3 + y2z3))\\
&\quad\quad ((\cos^2(b) + (e-1)^2\sin^2(b))\cos^2(P) + (e-1)^2\sin^2(P))^2 +\\
&\quad \sqrt{\Big(4\Big(\text{xpt}\,((2-e)^2 e^2\cos(P)\cos^2(b)\sin(2P)\sin(2b) - 2(e-2)(e-1)^2 e\sin(P)\sin(2b))(x2y1 - x3y1 - x1y2 + x3y2 + x1y3 - x2y3)^2 -\\
&\quad\quad 2(2-e)e((\cos^2(b) + (e-1)^2\sin^2(b))\cos^2(P) + (e-1)^2\sin^2(P))\\
&\quad\quad\quad ((x3y2z1 - x2y3z1 - x3y1z2 + x1y3z2 + x2y1z3 - x1y2z3 + \text{xpt}(-y2z1 + y3z1 + y1z2 - y3z2 - y1z3 + y2z3))\\
&\quad\quad\quad\quad \sin(2P)\cos^2(b) + \text{xpt}(x2z1 - x3z1 - x1z2 + x3z2 + x1z3 - x2z3)\cos(P)\sin(2b))\\
&\quad\quad\quad (x2y1 - x3y1 - x1y2 + x3y2 + x1y3 - x2y3) + 4(x2z1 - x3z1 - x1z2 + x3z2 + x1z3 - x2z3)\\
&\quad\quad\quad (x3y2z1 - x2y3z1 - x3y1z2 + x1y3z2 + x2y1z3 - x1y2z3 + \text{xpt}(-y2z1 + y3z1 + y1z2 - y3z2 - y1z3 + y2z3))\\
&\quad\quad\quad ((\cos^2(b) + (e-1)^2\sin^2(b))\cos^2(P) + (e-1)^2\sin^2(P))^2\Big)\text{\^{}}2 -\\
&\quad\quad 4\Big(((2-e)^2 e^2\sin^2(2P)\cos^4(b) + 2(e-1)^2((e-2)e - (e-2)\cos(2b)e + 2))(x2y1 - x3y1 - x1y2 + x3y2 + x1y3 - x2y3)^2 -\\
&\quad\quad\quad 4(2-e)e(x2z1 - x3z1 - x1z2 + x3z2 + x1z3 - x2z3)\cos^2(b)\sin(2P)\\
&\quad\quad\quad ((\cos^2(b) + (e-1)^2\sin^2(b))\cos^2(P) + (e-1)^2\sin^2(P))(x2y1 - x3y1 - x1y2 + x3y2 + x1y3 - x2y3) +\\
&\quad\quad\quad 4(x2z1 - x3z1 - x1z2 + x3z2 + x1z3 - x2z3)^2((\cos^2(b) + (e-1)^2\sin^2(b))\cos^2(P) + (e-1)^2\sin^2(P))^2\Big)\\
&\quad\quad \Big(((e-2)e(2\cos(2P)\cos^2(b) + \cos(2b))a^2 - a^2(3(e-2)e + 4) +\\
&\quad\quad\quad\quad \text{xpt}^2(-2(e-2)e\cos(2P)\cos^2(b) + (e-2)e + (e-2)e\cos(2b) + 4))(e-1)^2 + (2-e)^2 e^2\,\text{xpt}^2\cos^2(P)\sin^2(2b))\\
&\quad\quad\quad (x2y1 - x3y1 - x1y2 + x3y2 + x1y3 - x2y3)^2 -\\
&\quad\quad\quad 4(2-e)\,\text{expt}\,(x3y2z1 - x2y3z1 - x3y1z2 + x1y3z2 + x2y1z3 - x1y2z3 +\\
&\quad\quad\quad\quad \text{xpt}(-y2z1 + y3z1 + y1z2 - y3z2 - y1z3 + y2z3))\cos(P)((\cos^2(b) + (e-1)^2\sin^2(b))\cos^2(P) + (e-1)^2\sin^2(P))\\
&\quad\quad\quad \sin(2b)(x2y1 - x3y1 - x1y2 + x3y2 + x1y3 - x2y3) +\\
&\quad\quad\quad 4(x3y2z1 - x2y3z1 - x3y1z2 + x1y3z2 + x2y1z3 - x1y2z3 + \text{xpt}(-y2z1 + y3z1 + y1z2 - y3z2 - y1z3 + y2z3))^2\\
&\quad\quad\quad ((\cos^2(b) + (e-1)^2\sin^2(b))\cos^2(P) + (e-1)^2\sin^2(P))^2\Big)\Big)\Big)\Big/\\
&\Big(2\Big(((2-e)^2 e^2\sin^2(2P)\cos^4(b) + 2(e-1)^2((e-2)e - (e-2)\cos(2b)e + 2))(x2y1 - x3y1 - x1y2 + x3y2 + x1y3 - x2y3)^2 -\\
&\quad\quad 4(2-e)e(x2z1 - x3z1 - x1z2 + x3z2 + x1z3 - x2z3)\cos^2(b)\sin(2P)((\cos^2(b) + (e-1)^2\sin^2(b))\cos^2(P) + (e-1)^2\sin^2(P))\\
&\quad\quad (x2y1 - x3y1 - x1y2 + x3y2 + x1y3 - x2y3) + 4(x2z1 - x3z1 - x1z2 + x3z2 + x1z3 - x2z3)^2\\
&\quad\quad ((\cos^2(b) + (e-1)^2\sin^2(b))\cos^2(P) + (e-1)^2\sin^2(P))^2\Big)\Big)\Big];
\end{aligned}
$$

```
newyintc = Compile[{a, e, b, P, {zpt, _Real, 1}, x1, x2, x3, y1, y2, y3, z1, z2, z3},
  (2(-y2z1 + y3 z1 + y1 z2 - y3 z2 - y1 z3 + y2 z3)
      (-2(e - 2)(e - 1)^2 e(-y2z1 + y3z1 + y1 z2 - y3z2 - y1 z3 + y2z3)zpt sin(2 P) cos^2(b) +
        (e - 2)^2 e^2 (-y2z1 + y3 z1 + y1z2 - y3 z2 - y1z3 + y2z3) zptcos(P) sin^2(2b)sin(P) +
        (e - 2)e(-x3 y2z1 + x2 y3z1 + x3 y1z2 - x1 y3z2 - x2 y1z3 + x1y2 z3 + (x2y1 - x3y1 - x1 y2 + x3y2 + x1 y3 - x2y3)zpt)
         ((e - 2) e + (e - 2)cos(2b)e + 2)sin(2b) sin(P)) +
    2(-x2 z1 + x3z1 + x1 z2 - x3z2 - x1z3 + x2 z3)((e - 2)e + (e - 2)cos(2b)e + 2)
     ((-x3y2 z1 + x2y3 z1 + x3y1 z2 - x1y3 z2 - x2y1 z3 + x1y2 z3) (-(e - 2) e - (e - 2)cos(2b)e - 2) -
       zpt ((x2y1 - x3y1 - x1 y2 + x3y2 + x1 y3 - x2y3)((e - 2)e + (e - 2) cos(2b) e + 2) +
         (e - 2)e (-y2 z1 + y3z1 + y1z2 - y3 z2 - y1z3 + y2z3) cos(P) sin(2b))) +
    √(4((-x2z1 + x3 z1 + x1z2 - x3 z2 - x1z3 + x2z3) ((e - 2)e + (e - 2) cos(2 b)e + 2)
          ((-x3 y2z1 + x2 y3z1 + x3 y1z2 - x1 y3z2 - x2 y1z3 + x1 y2z3) ((e - 2)e + (e - 2)cos(2 b)e + 2) + zpt
            ((x2y1 - x3 y1 - x1y2 + x3y2 + x1 y3 - x2y3) ((e - 2)e + (e - 2)cos(2b) e + 2) +
              (e - 2) e(-y2z1 + y3 z1 + y1z2 - y3 z2 - y1z3 + y2z3)cos(P) sin(2 b))) -
        (-y2z1 + y3 z1 + y1z2 - y3 z2 - y1z3 + y2z3)
          (-2 (e - 2)(e - 1)^2 e(-y2z1 + y3z1 + y1z2 - y3 z2 - y1z3 + y2 z3) zptsin(2 P)cos^2(b) + (e - 2)^2 e^2
            (-y2z1 + y3 z1 + y1z2 - y3z2 - y1 z3 + y2z3) zptcos(P) sin^2(2b)sin(P) + (e - 2) e
            (-x3y2 z1 + x2y3 z1 + x3y1 z2 - x1y3 z2 - x2y1 z3 + x1y2 z3 +
              (x2y1 - x3 y1 - x1y2 + x3 y2 + x1y3 - x2 y3) zpt) ((e - 2) e + (e - 2)cos(2b) e + 2) sin(2 b)sin(P)))^ 2 -
      4((e - 1)^2 (-2((e - 2)e + 2)a^2 - 2(e - 2) ecos(2 b)a^2 + zpt^2 (-2(e - 2)ecos(2 P) cos^2(b) + (e - 2)e + (e - 2) ecos(2b) + 4))
          (-y2z1 + y3 z1 + y1z2 - y3 z2 - y1z3 + y2z3)^2 +
        (-x3y2 z1 + x2y3 z1 + x3y1 z2 - x1y3 z2 - x2y1 z3 + x1y2 z3)^2 ((e - 2)e + (e - 2) cos(2b) e + 2)^2 +
        zpt^2 ((x2y1 - x3y1 - x1 y2 + x3 y2 + x1y3 - x2 y3)((e - 2)e + (e - 2)cos(2b)e + 2) + (e - 2) e
            (-y2z1 + y3 z1 + y1z2 - y3z2 - y1 z3 + y2z3) cos(P) sin(2b))^ 2 +
        2(-x3y2z1 + x2y3z1 + x3y1z2 - x1y3z2 - x2y1z3 + x1y2 z3)zpt ((e - 2)e + (e - 2) cos(2 b)e + 2)
         ((x2y1 - x3 y1 - x1y2 + x3 y2 + x1y3 - x2y3) ((e - 2)e + (e - 2)cos(2b)e + 2) +
           (e - 2) e(-y2z1 + y3 z1 + y1z2 - y3 z2 - y1z3 + y2z3) cos(P) sin(2b)))
       ((((e - 2) e + (e - 2)(2cos(2 P) cos^2(b) + cos(2 b))e + 4)(e - 1)^2 + (e - 2)^2 e^2 sin^2(2b)sin^2(P))
         (-y2z1 + y3 z1 + y1z2 - y3 z2 - y1z3 + y2z3)^2 - 2(e - 2)e (-x2z1 + x3 z1 + x1z2 - x3 z2 - x1 z3 + x2z3)
         ((e - 2)e + (e - 2)cos(2b)e + 2) sin(P) sin(2b)(-y2 z1 + y3z1 + y1z2 - y3 z2 - y1z3 + y2 z3) +
        (-x2z1 + x3 z1 + x1z2 - x3 z2 - x1z3 + x2 z3)^2 ((e - 2)e + (e - 2)cos(2b)e + 2)^2))) /
  (2(((e - 2)e + (e - 2) (2cos(2 P)cos^2(b) + cos(2b))e + 4)(e - 1)^2 + (e - 2)^2 e^2 sin^2(2b)sin^2(P))
     (-y2z1 + y3 z1 + y1z2 - y3 z2 - y1z3 + y2 z3)^2 -
    4(e - 2)e(-x2 z1 + x3z1 + x1 z2 - x3z2 - x1 z3 + x2 z3) ((e - 2) e + (e - 2)cos(2b)e + 2)sin(P) sin(2 b)
     (-y2z1 + y3 z1 + y1z2 - y3 z2 - y1z3 + y2 z3) + 2(-x2 z1 + x3z1 + x1 z2 - x3z2 - x1z3 + x2z3)^2 ((e - 2)e + (e - 2)cos(2b) e + 2)^2)];
```

Above is Equation B, with variables defined the same as in Equation A, with the exception that *zpt* is the z-coordinate of the point of interest. By inputting *zpt* into Equation B, the corresponding y-coordinate of that point is calculated.

APPENDIX B

The following Mathematica, IDL, and CAD files were used in the production of the tables and figures in this paper.

Figure 1: LOWELL:Local Files:Theses:Hilbert 2001:Figures:refrac and refracCAD

Figure 2: LOWELL:Local Files:Projects:Jupiter:HIP9369:LightCurve Fits:IRTFIm3Dfit6.nb

Figure 3: LOWELL:Local Files:Theses:Hilbert 2001:Figures:osculating_circle2
and osculating_circle2CAD

Figure 4: LOWELL:Local Files:Theses:Hilbert 2001:Figures:LOSdefinition
and LOSdefinitionCAD

Figure 5:LOWELL:Local Files :Theses:Hilbert 2001:Figures:
hubbardfits1.0.nb
HLC_plotBS.nb

Figure 6: LOWELL:Local Files:Projects:Jupiter:HIP9369:Line of sight ellipticity:
E=0.06487TIP0.3.nb
E=0.06487TIP5.3.nb
E=0.06487TIP10.3.nb
E=0.06487TIP20.3.nb
E=0.06487TIP25.3.nb
E=0.06487TIP30.3.nb

E=0.06487TIP35.3.nb

E=0.06487TIP45.3.nb

Figure 7: LOWELL:Local Files:Projects:Jupiter:HIP9369:Inversions:test cases:final latitude test cases:

E=0.06487_EQ_ISO8.0.nb

Figure 8: LOWELL:Local Files:Projects:Jupiter:HIP9369:Inversions:test cases:final latitude test cases:

E=0.06487_EQ_ISO8.0.nb

E=0.06487_15RAD_ISO6.0.nb

E=0.06487_30RAD_ISO6.0.nb

E=0.06487_45RAD_ISO5.0.nb

E=0.06487_60RAD_ISO5.0.nb

E=0.06487_75RAD_ISO5.0.nb

E=0.06487_POL_ISO5.0.nb

SVInv44.4.nb

Table 1: LOWELL:Local Files:Projects:Jupiter:HIP9369:Numerical Integration:

LastEllIntegration49.0.nb

Table 2:LOWELL:Local Files :Theses:Hilbert 2001:Figures:hubbardfits1.0.nb

Table 3: LOWELL:Local Files:Projects:Jupiter:HIP9369:Line of sight ellipticity:

E=0.06487TIP0.3.nb

REFERENCES

Baum, W. A., and A. D. Code 1953. A photometric observation of the occultation of s Arietis by Jupiter. *Astron. J.* **58**, 108-112.

Chamberlain, D. M., and J. L. Elliot 1997. A Numerical Method for Calculating Occultation Light Curves from an Arbitrary Atmospheric Model. *Publ. Astron. Soc. Pacific* **109**, 1170-1180.

Cooray, A. R., J. L. Elliot, A. S. Bosh, L. A. Young, and M. A. Shure 1998. Stellar occultation observations of Saturn's north-polar temperature structure. *Icarus* **132**, 298-310.

Elliot, J. L., A. S. Bosh, M. L. Cooke, R. C. Bless, M. J. Nelson, J. W. Percival, M. J. Taylor, J. F. Dolan, E. L. Robinson, and G. W. van Citters 1993. An occultation by Saturn's rings on 1991 October 2-3 observed with the Hubble Space Telescope. *Astron. J.* **106**, 2544-2572.

Elliot, J. L., and C. B. Olkin 1996. Probing Planetary Atmospheres with Stellar Occultations. In *Annual Review of Earth and Planetary Sciences* (G. W. Wetherill, Ed.), pp. 89-123. Annual Reviews Inc., Palo Alto.

Elliot, J. L., and L. A. Young 1992. Analysis of stellar occultation data for planetary atmospheres. I. Model fitting, with application to Pluto. *Astron. J.* **103**, 991-1015.

French, R. G., J. L. Elliot, and P. J. Gierasch 1978. Analysis of stellar occultation data. Effects of photon noise and initial conditions. *Icarus* **33**, 186-202.

Hubbard, W. B., C. C. Porco, D. M. Hunten, G. H. Rieke, M. J. Rieke, D. W. McCarthy, V. Hammerle, J. Haller, B. McLeod, L. A. Lebofsky, R. L. Marcialis, J. B. Holberg, R. Landau, L. Carrasco, J. Elias, M. W. Buie, E. W. Dunham, S. E. Persson, T. Boroson, S. West, R. G. French, J. Harrington, J. L. Elliot, W. J. Forrest, J. L. Pipher, R. J. Stover, B. Sicardy, A. Brahic, and I. Grenier 1997. Structure of Saturn's mesopshere from the 28 Sgr occultations. *Icarus* **130**, 404-425.

Roques, F., B. Sicardy, R. G. French, W. B. Hubbard, A. Barucci, P. Bouchet, A. Brahic, J.-A. Gehrels, T. Gehrels, I. Grenier, T. Lebertre, J. Lecacheux, J. P. Maillard, R. A. McLaren, C. Perrier, F. Vilas, and M. D. Waterworth 1994. Neptune's upper stratosphere, 1983-1990: Ground-based stellar occultation observations. *Astron. & Astrophys.* **288**, 985-1011.

USNO 1999. *The Astronomical Almanac for the Year 1999.* U.S. Government Printing Office, Washington D.C.